Timescales of hydrothermal scavenging in the South Pacific Ocean from 234 Th, 230 Th, and 228 Th

Frank J Pavia, Robert F Anderson, Erin E Black, Lauren E Kipp, Sebastian M Vivancos, Martin Q Fleisher, Matthew A Charette, Virginie Sanial, Willard S Moore, Mikael Hult, et al.

Pavia, F. J., Anderson, R. F., Black, E. E., Kipp, L. E., Vivancos, S. M., Fleisher, M. Q., Charette, M. A., Sanial, V., Moore, W. S., Hult, M., Lu, Y., Cheng, H., Zhang, P. and Edwards, R. L.: Timescales of hydrothermal scavenging in the South Pacific Ocean from 234Th, 230Th, and 228Th, Earth and Planetary Science Letters, 506, 146–156, doi:10.1016/j.epsl.2018.10.038, 2019.

Timescales of hydrothermal scavenging in the South Pacific Ocean from ^{234}Th, ^{230}Th, and ^{228}Th

Frank J. Pavia [a,b,*], Robert F. Anderson [a,b], Erin E. Black [c,d], Lauren E. Kipp [c,d], Sebastian M. Vivancos [a,b], Martin Q. Fleisher [a], Matthew A. Charette [d], Virginie Sanial [e], Willard S. Moore [f], Mikael Hult [g], Yanbin Lu [h], Hai Cheng [h,i], Pu Zhang [h], R. Lawrence Edwards [h]

[a] *Lamont-Doherty Earth Observatory of Columbia University, Palisades, NY, USA*
[b] *Department of Earth and Environmental Sciences, Columbia University, New York, NY, USA*
[c] *Massachusetts Institute of Technology/Woods Hole Oceanographic Institution Joint Program in Oceanography/Applied Ocean Science and Engineering, USA*
[d] *Department of Marine Chemistry and Geochemistry, Woods Hole Oceanographic Institution, Woods Hole, MA 02543, USA*
[e] *Division of Marine Science, University of Southern Mississippi, Stennis Space Center, MS 39529, USA*
[f] *Department of Earth and Ocean Sciences, University of South Carolina, Columbia, SC 29208, USA*
[g] *European Commission, Joint Research Centre, Directorate for Nuclear Safety and Security, Geel, Belgium*
[h] *Department of Earth Sciences, University of Minnesota, Minneapolis, MN, USA*
[i] *Institute of Global Environmental Change, Xi'an Jiaotong University, Xi'an, China*

ARTICLE INFO

Article history:
Received 3 May 2018
Received in revised form 23 October 2018
Accepted 26 October 2018
Available online xxxx
Editor: D. Vance

Keywords:
thorium
hydrothermal activity
scavenging
GEOTRACES
East Pacific Rise

ABSTRACT

Hydrothermal activity in the deep ocean generates plumes of metal-rich particles capable of removing certain trace elements from seawater by adsorption and sedimentation. This removal process, known as scavenging, can be probed using the insoluble radiogenic isotopes of thorium (Th), which are produced at a known rate in the water column via the decay of soluble uranium (^{234}Th, ^{230}Th) and radium (^{228}Th) isotopes. We present dissolved and particulate measurements of these three thorium isotopes in a hydrothermal plume observed in the southeast Pacific Ocean on the GEOTRACES GP16 section. Since their half-lives vary from days (^{234}Th) to years (^{228}Th) to tens of thousands of years (^{230}Th), the combination of their signals can be used to understand scavenging processes occurring on a wide range of timescales. Scavenging is a multi-step process involving adsorption and desorption onto particles, followed by particle aggregation, sinking, and eventual sedimentation. We use thorium isotopes to study how hydrothermal activity affects these steps. The rate constants for net adsorption of ^{234}Th determined here are comparable to previous estimates from hydrothermal plumes in the Atlantic and North Pacific Oceans. The partitioning of ^{234}Th and ^{230}Th between large and small particles is more similar in the hydrothermal plume than above it, indicating faster aggregation of particles within the hydrothermal plume at stations nearby the East Pacific Rise than in waters outside the plume. In addition to rapid scavenging and aggregation near the ridge axis, we also infer continuous off-axis scavenging from observations and modeling of ^{228}Th/^{228}Ra activity ratios. The degree of depletion of the three thorium isotopes increases in order of half-life, with total ^{234}Th activity close to that of its parent ^{238}U, but ^{230}Th showing nearly 70% depletion compared to expected values from reversible scavenging. By modeling the variations in depletion for the different isotopes, we show that much of the ^{230}Th removal is inherited from scavenging events happening long before the most recent hydrothermal inputs.

1. Introduction

Submarine hydrothermal vents emit hot, reducing fluids that are highly enriched in trace metals such as iron (Fe) and manganese (Mn) relative to the deep ocean (German and Seyfried, 2014). Upon reacting with seawater, dissolved Fe and Mn precipitate to form particles, with Fe initially forming sulfides closest to the ridge axis (e.g. Feely et al., 1987), and both Fe and Mn forming oxides over longer distances (Feely et al., 1996). These metalliferous particles have highly reactive surfaces that can readily remove trace metals, phosphorus, and carbon from solution (Feely et al.,

* Corresponding author at: Lamont-Doherty Earth Observatory of Columbia University, Palisades, NY, USA.
E-mail address: fpavia@ldeo.columbia.edu (F.J. Pavia).

1990; German et al., 2015; Kadko et al., 1994), making hydrothermal systems important sinks for a wide range of elements in the ocean.

The south Pacific was identified as a major locality of hydrothermal activity by the discovery of volcanic ^{3}He emanating from the East Pacific Rise (EPR) at 2500 m between 15°–20°S (Lupton and Craig, 1981). In 2013, the GEOTRACES GP16 cruise followed this south Pacific helium plume west of the EPR. In addition to ^{3}He, the plume was found to be highly enriched in dissolved metals like Fe (dFe) and Mn (dMn) over 4000 km west of the EPR (Resing et al., 2015). Enrichments in particulate Fe (pFe) and Mn (pMn) were also found in the GP16 hydrothermal plume (Fitzsimmons et al., 2017). While pMn and dMn were both found to have peaks along the same isopycnal as ^{3}He, the pFe and dFe peaks descended below the ^{3}He isopycnal, indicating removal by sinking particles, despite the apparent conservative behavior of dFe previously inferred by Resing et al. (2015). Modeling studies have shown that hydrothermal Fe, stabilized in solution and carried by abyssal ocean circulation, could upwell and support new primary production, particularly in the Southern Ocean (Resing et al., 2015; Tagliabue et al., 2010). A better understanding of removal processes and their associated timescales in hydrothermal plumes could potentially improve models of Fe stabilization and removal.

Chemical scavenging encapsulates the sum of processes responsible for the removal of ions from the ocean by oceanic particles. These individual processes include adsorption and desorption reactions, aggregation and disaggregation of particles, and eventually particle settling and sedimentation at the seafloor (Bacon and Anderson, 1982). Net scavenging rates responsible for the removal of elements from the ocean integrate across the rates of these individual processes.

The radiogenic isotopes of thorium (^{234}Th, ^{230}Th, ^{228}Th) are powerful tools for understanding the kinetics of oceanic scavenging processes. These thorium isotopes are produced at well-known rates in seawater by the decay of soluble uranium (^{238}U $\rightarrow$ ^{234}Th, ^{234}U $\rightarrow$ ^{230}Th) and radium (^{228}Ra $\rightarrow$ ^{228}Th). Thorium is highly insoluble in seawater, with a scavenging residence time on the order of 10–40 yr in the deep ocean (Henderson and Anderson, 2003). Thorium adsorbs onto particles that subsequently settle through the water column, generating radioactive disequilibrium with respect to their more soluble parents. The rapid removal of Th is apparent from the open ocean activity ratio of ^{230}Th to its parent ^{234}U of ~0.00002 (Moore and Sackett, 1964). With respective half-lives for ^{234}Th, ^{230}Th, and ^{228}Th of 24.1 days (Knight and Macklin, 1948), 75,587 yr (Cheng et al., 2013), and 1.91 yr (Kirby et al., 1956), thorium isotopes can constrain scavenging behavior in the ocean on a range of timescales spanning months to millennia.

Pavia et al. (2018) studied hydrothermal scavenging of ^{230}Th and ^{231}Pa in the GP16 hydrothermal plume, finding large depletions in total and dissolved ^{230}Th and ^{231}Pa coincident with enrichments in the particulate phase. The authors determined that this intense scavenging was largely the result of iron and manganese coatings on particles, and that scavenging was continuous over the 4000 km extent of the plume. In this study, we use combined measurements of dissolved and particulate ^{234}Th, ^{230}Th, and ^{228}Th and their parent activities to study the kinetics of the individual processes involved in scavenging, including adsorption and desorption, particle aggregation, and the net scavenging removal of thorium from the water column. We use these observations to assess the importance of local and distal hydrothermal activity on ^{230}Th scavenging previously observed in the GP16 hydrothermal plume, and to study the timescales over which different scavenging processes act in hydrothermal settings.

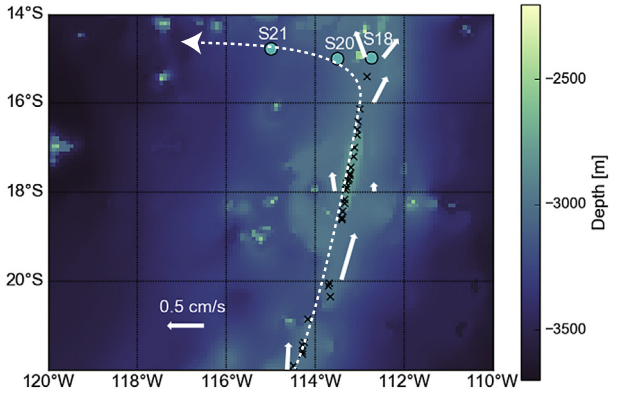

Fig. 1. Site map of the study area. Net velocities of RAFOS floats deployed along the EPR (Hautala and Riser, 1993; Lupton and Jenkins, 2017) are shown as solid white arrows. Sampling sites discussed in this paper are teal dots. Locations of active hydrothermal vent sites (http://vents-data.interridge.org) are shown as black X marks. Dashed white arrow shows proposed flow path of waters entering the GP16 off-axis hydrothermal plume discussed in Section 4.3.

2. Materials and methods

2.1. Cruise setting

Samples were taken on board the *R.V. Thomas G. Thompson* during the GEOTRACES GP16 cruise (TGT303) between Ecuador and Tahiti from 25 October to 20 December, 2013. We focus on the three sampling locations at or nearest downstream of the EPR: station 18 at the EPR and stations 20 and 21, less than 250 km to the west along 15°S latitude (Fig. 1). Since the hydrothermal plume was interrupted by a discontinuity due to mixing of non-plume waters at the next station to the west (Jenkins et al., 2018; Lupton and Jenkins, 2017), we restrict our analysis to the three stations nearest to the EPR.

2.2. Sample collection and analysis

Dissolved ^{230}Th and total ^{234}Th samples were taken from Niskin bottles, with ^{230}Th collected from bottles on a conventional steel rosette and deep ^{234}Th samples taken from bottles hung above *in-situ* pumps. Dissolved ^{228}Th and ^{228}Ra samples were collected by pumping water filtered at 0.8 µm over in-line QMA and Supor filters using McLane *in-situ* pumps, and then over MnO_2 coated acrylic cartridges (Henderson et al., 2013; Maiti et al., 2015). Particulate samples for all Th isotopes were collected via battery-operated McLane *in-situ* pumps in two size classes: 0.8–51 µm, the small size fraction (SSF) and >51 µm, the large size fraction (LSF). All data from the GEOTRACES GP16 section presented in this paper are available in the 2017 GEOTRACES Intermediate Data Product (https://www.bodc.ac.uk/geotraces/data/idp2017/). Much of the data is also archived at the Biological and Chemical Oceanography Data Management Office (BCO-DMO), including total ^{234}Th and ^{238}U (https://www.bco-dmo.org/dataset/643213), particulate ^{234}Th (https://www.bco-dmo.org/dataset/643316), dissolved ^{230}Th (https://www.bco-dmo.org/dataset/643639), particulate ^{230}Th (https://www.bco-dmo.org/dataset/676231), and ^{228}Ra (https://www.bco-dmo.org/dataset/650340).

2.2.1. ^{234}Th

The methods for analyzing GP16 samples for total and particulate ^{234}Th have been summarized previously (Black et al., 2018). Briefly, 4 L samples for analysis of total ^{234}Th were spiked with ^{230}Th as a yield monitor, pre-concentrated by co-precipitation with MnO_2, and collected on Whatman quartz microfiber (QMA) filters. Particulate ^{234}Th samples were taken in two size fractions

using *in-situ* pumps. The LSF particles were collected onto a prefilter, and rinsed onto silver filters. SSF particles were filtered onto QMA filters. The activity of ^{234}Th for both total and particulate samples was determined using anti-coincidence beta counters and corrected for background radioactivity. To compute the radioactive disequilibrium of ^{234}Th, ^{238}U was predicted for each sample by the U-salinity relationship of Owens et al. (2011). Dissolved ^{234}Th is calculated as the difference between the total and particulate pools.

2.2.2. ^{230}Th

The ^{230}Th data and methods in this paper have been previously published (Pavia et al., 2018). Seawater samples (~5 L) were filtered over 0.45 µm Acropak capsule filters at sea and acidified to pH = 2 using redistilled 6M hydrochloric acid for storage and on-shore analysis. Size-fractionated particulate ^{230}Th samples were taken using *in-situ* pumps, with LSF particles collected on a Sefar polyester mesh prefilter, and SSF particles collected on paired 0.8 µm Supor filters. Dissolved samples were spiked with ^{229}Th, co-precipitated using iron oxyhydroxide, then digested using HF, HNO_3, and $HClO_4$. Particulate samples were spiked with ^{229}Th and dissolved using HNO_3 and $HClO_4$, followed by iron co-precipitation and subsequent redissolution. For both dissolved and particulate samples, thorium isotopes were then separated using anion exchange chromatography (BioRad AG1-X8). Concentrations of ^{230}Th were determined on a Thermo ELEMENT XR single collector inductively-coupled plasma mass spectrometer in peak jumping mode. Dissolved ^{230}Th data presented here have been corrected for detrital ^{230}Th present in the dissolved pool from the dissolution of continental material (e.g. Roy-Barman et al., 2009), and ingrowth from ^{234}U decay during sample storage. The ^{234}U activity in each sample was computed by multiplying the ^{238}U-salinity relationship (Owens et al., 2011) by the oceanic ^{234}U/^{238}U activity ratio of 1.1468 (Andersen et al., 2010).

2.2.3. ^{228}Th and ^{228}Ra

Filtered seawater was pumped over MnO_2-coated cellulose filters by McLane *in-situ* pumps to collect dissolved ^{228}Th and ^{228}Ra samples. Typically, 1500–1700 L of seawater was filtered at an average flow rate of 6.5 L min^{-1} with an average cartridge collection efficiency of 66 ± 17%. Particulate samples were collected in the SSF on QMA filters via the same *in-situ* pumps. Full procedures for the analysis of ^{228}Ra on the GP16 section have been published (Kipp et al., 2018b). The MnO_2 cartridges and QMA filters were counted for ^{228}Th via ^{220}Rn emanation with the RaDeCC alpha delayed coincidence system (Charette et al., 2015; Maiti et al., 2015; Moore and Arnold, 1996). This method detects adsorbed ^{228}Th capable of releasing ^{220}Rn; the resulting particulate activity should therefore be considered a lower limit, as there may be additional ^{228}Th in phases that trap its ^{220}Rn from being released. For dissolved samples, after RaDeCC analysis, the MnO_2-coated cartridges were ashed and gamma counted for ^{234}Th and ^{226}Ra on high purity, well-type germanium detectors. The cartridge-based ^{234}Th and ^{226}Ra measurements were compared to small-volume (~4 L) beta counting measurements of ^{234}Th and ^{226}Ra collected from Niskin bottles hung at the depth of each sample, and the ratio of ^{234}Th and ^{226}Ra measured on the small-volume samples to that measured on the MnO_2-coated cartridges was used to calculate the collection efficiency of ^{228}Th and ^{228}Ra on the cartridges (Maiti et al., 2015).

^{228}Ra activities were measured on gamma detectors located underground at the Laboratoire Souterrain de Modane in France and the HADES laboratory in Belgium. The underground location of these laboratories serves to minimize the amount of cosmic radiation reaching the detectors, reducing the detection limits.

3. Results

At stations 18 and 20 there is a clear signature of hydrothermal scavenging observed in the profiles of all three thorium isotopes below 2200 m (Fig. 2). The most distinct signal for the shorter lived ^{234}Th and ^{228}Th is enrichment in the particulate phase. In background, non-plume influenced deep waters, particulate ^{234}Th makes up less than 5% of the total ^{234}Th, with activities of 1.4–1.8 mBq/kg. In the hydrothermal plume at stations 18 and 20, particulate ^{234}Th reaches a peak of 32% of the total pool and consistently has activities of 9–12 mBq/kg. Particulate ^{230}Th increases from background values near 2 µBq/kg to more than 4 µBq/kg, reaching 57% of the total pool. Particulate ^{228}Th increases from 0.1–0.5 µBq/kg in non-plume waters to 3.5–4.5 µBq/kg within the plume, peaking at 36% of the total ^{228}Th. At station 21, there is a slight enrichment in particulate ^{234}Th to 3.97 mBq/kg and in particulate ^{228}Th to 1.76 µBq/kg.

There is little sign of significant excess in or deficit of total ^{234}Th relative to its parent ^{238}U. A steady state mass balance model of ^{234}Th can be used to determine scavenging and removal rates of ^{234}Th in hydrothermal plumes (Kadko, 1996). The mass budget for dissolved ^{234}Th can be written:

$$\frac{\partial {}^{234}\mathrm{Th}_{diss}}{\partial t} = \left({}^{238}\mathrm{U} - {}^{234}\mathrm{Th}_{diss}\right)\lambda - J_{\mathrm{Th}} \quad (1)$$

where ^{238}U is the dissolved ^{238}U inventory (Bq/m^2) in the plume, defined here as the depth interval between 2200 and 3000 m, $^{234}\mathrm{Th}_{diss}$ is dissolved ^{234}Th inventory (Bq/m^2) in the plume, λ is the decay constant of ^{234}Th in yr^{-1} and J_{Th} is the net rate at which dissolved ^{234}Th is adsorbed onto particles in Bq m^{-2} yr^{-1}. Assuming steady state, we can solve for J_{Th}, then the net adsorption rate constant of ^{234}Th in the plume (k_1, in units yr^{-1}) by dividing the scavenging rate by the dissolved ^{234}Th inventory:

$$k_1 = \frac{J_{\mathrm{Th}}}{{}^{234}\mathrm{Th}_{diss}} \quad (2)$$

At station 18, we derive $J_{\mathrm{Th}} = 106 \pm 16$ Bq m^{-2} day^{-1} and $k_1 = 2.99 \pm 0.47$ yr^{-1}. At station 20, we find $J_{\mathrm{Th}} = 147 \pm 31$ Bq m^{-2} day^{-1} and $k_1 = 2.32 \pm 0.51$ yr^{-1}. At station 21, J_{Th} and k_1 decrease to 35.5 ± 17 Bq m^{-2} day^{-1} and 1.21 ± 0.58 yr^{-1} respectively. Our estimates of J_{Th} are comparable to previous values of 152 Bq m^{-2} day^{-1} found by Owens et al. (2015) at the Mid-Atlantic Ridge and 81.6–202 Bq m^{-2} day^{-1} found by Kadko et al. (1994) at the Juan de Fuca Ridge.

Unlike ^{234}Th, there is a large deficit of total ^{230}Th in the hydrothermal plume at stations 18–21 relative to the concentration profiles expected for removal by reversible scavenging. Reversible scavenging should drive dissolved, particulate, and total ^{230}Th activities to linearly increase with depth throughout the water column (Bacon and Anderson, 1982). Above the hydrothermal plume this is the case along GP16 (Pavia et al., 2018); however, below 2200 m at stations 18–21, total ^{230}Th sharply declines from 15–17 µBq/kg to less than 5 µBq/kg (Fig. 2). A similar signal is seen in the dissolved phase, and the depletion of both total and dissolved ^{230}Th in the hydrothermal plume is roughly similar between the three stations. Whereas the imprint of hydrothermal scavenging signals on ^{234}Th essentially disappeared by station 21, roughly 250 km from the EPR, the hydrothermal depletion of dissolved and total ^{230}Th and enrichment of particulate ^{230}Th extends over 4000 km from the ridge axis (Pavia et al., 2018).

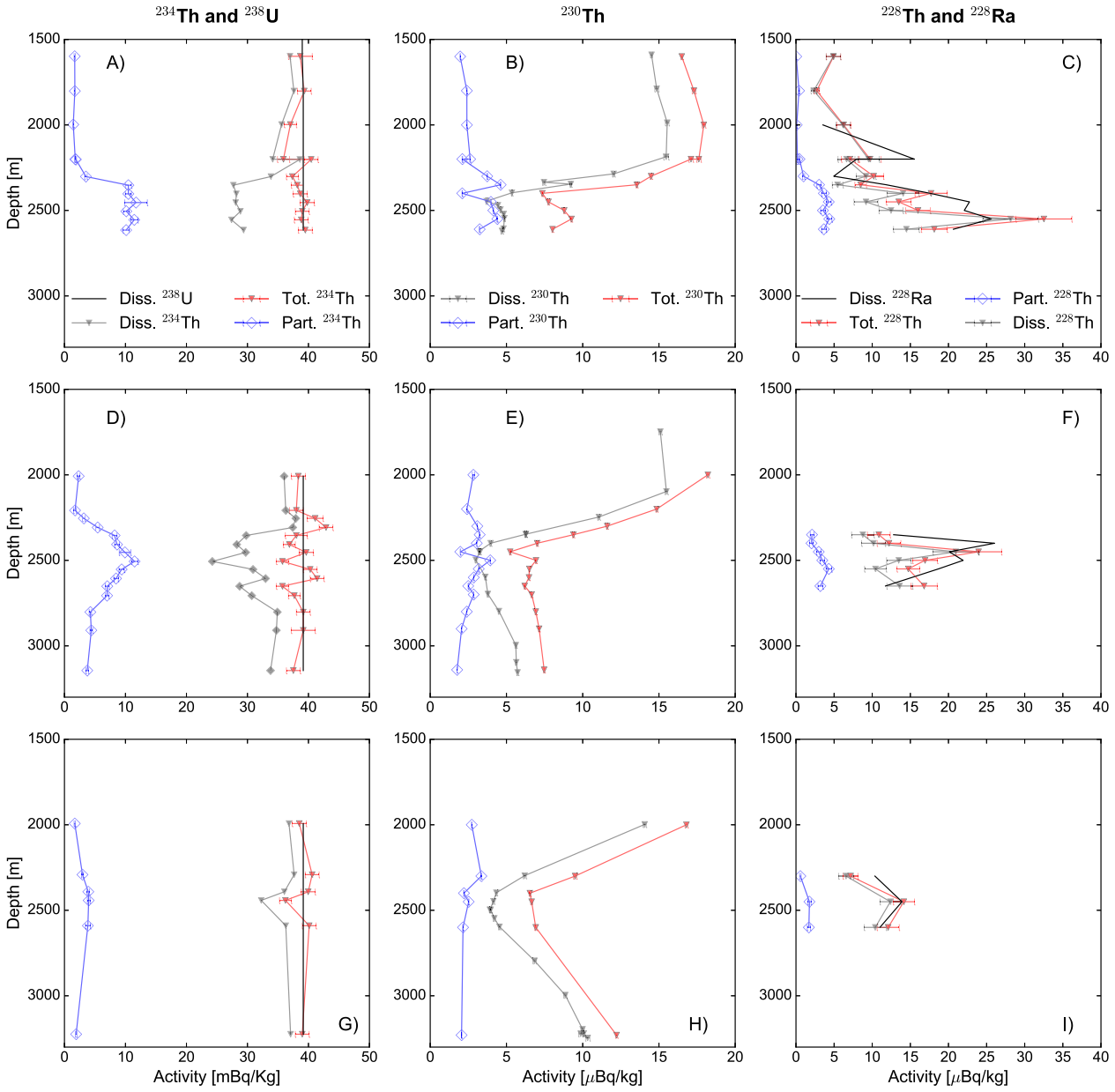

Fig. 2. Profiles of at station 18 (top row), station 20 (middle row), and station 21 (bottom row) of thorium isotopes and their parent activities from the GP16 section. Dissolved ^{238}U, and total, particulate, and dissolved ^{234}Th are shown in panels A, D, and G. Dissolved, particulate, and total ^{230}Th are shown in panels B, E, and H. Dissolved ^{228}Ra, and dissolved, particulate, and total ^{228}Th are shown in panels C, F, and I. Error bars represent 1-sigma uncertainty, and are smaller than the symbol size where not visible.

4. Discussion

4.1. Size partitioning of ^{234}Th and ^{230}Th

The isotopes of thorium are expected to have identical chemical scavenging behavior. Differences in observed scavenging intensities of the different isotopes can therefore be attributed to the different timescales over which they integrate, which are related to their half-lives. One of the key variables in determining the scavenging rates and sinking fluxes of particles is their size (Burd and Jackson, 2009). Smaller particles typically have a larger surface area to volume ratio, allowing for greater adsorption per unit mass of particles (Honeyman and Santschi, 1989), while larger particles are exported faster by gravitational settling (Burd and Jackson, 2009). Measuring thorium isotopes with varying half lives in particles of different size classes can be used to constrain the aggregation of small particles, with large surface area to mass ratios, into large particles that settle more rapidly.

On the GP16 section, particulate ^{234}Th measurements were made on both the LSF and SSF throughout the water column. Particulate ^{230}Th was mostly measured in the SSF, but there are 44 LSF measurements, including 17 in the hydrothermal plume at stations 18–21 that permit comparison with ^{234}Th. ^{228}Th was only measured in the SSF, so we can only compare the size partitioning of ^{234}Th and ^{230}Th. To do this, we use the fraction of thorium activity found in the large size fraction relative to the total particulate activity (Lee et al., 2018):

$$\mathrm{fLSF} = \frac{[\mathrm{pTh}]_{\mathrm{LSF}}}{([\mathrm{pTh}]_{\mathrm{LSF}} + [\mathrm{pTh}]_{\mathrm{SSF}})} \quad (3)$$

where [pTh] is the particulate activity of thorium. For the data available outside the hydrothermal plume, a slightly higher fraction

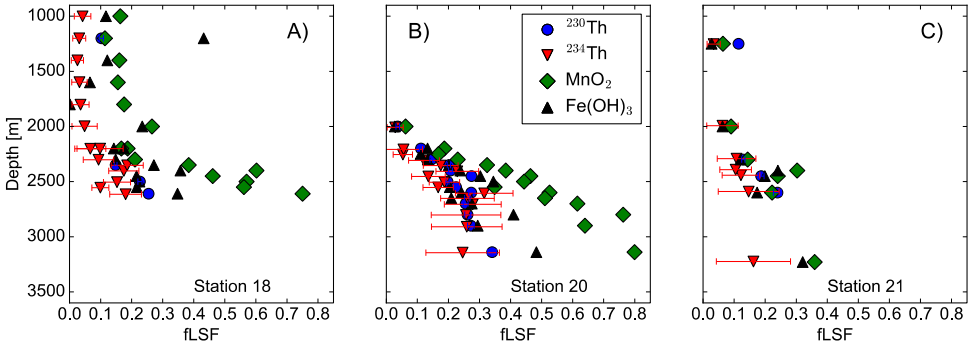

Fig. 3. Fractions of total particulate (sum of LSF and SSF size fractions) ^{230}Th (blue dots), ^{234}Th (red upside-down triangles), particulate MnO_2 (green diamonds), and particulate $Fe(OH)_3$ (black triangles) found in the large size fraction (>51 μm) from GP16 stations 18 (A), 20 (B), and 21 (C). $Fe(OH)_3$ and MnO_2 data from Lam et al. (2018). 1-Sigma uncertainties are shown for ^{234}Th and ^{230}Th and are smaller than the symbol size where not visible. (For interpretation of the colors in the figure(s), the reader is referred to the web version of this article.)

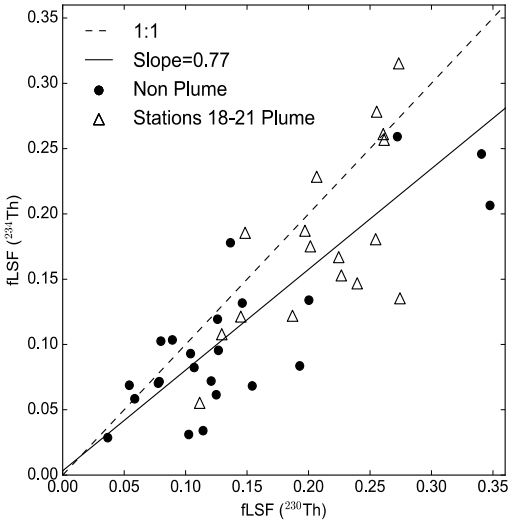

Fig. 4. Scatter plots of fLSF (fraction of total particulate thorium found in >51 μm particles, see Equation (3)) for ^{234}Th and ^{230}Th. Samples not in the hydrothermal plume (2200–3000 m) at stations 18, 20, and 21 are shown as dots. Samples within the hydrothermal plume as stations 18–21 are shown as open triangles. The dashed line shows the 1:1 line that would be expected if ^{234}Th and ^{230}Th were partitioned equally into the >51 μm size fraction. The solid line shows the best-fit linear slope of 0.77, indicating that ^{230}Th is preferentially incorporated into >51 μm particles in non-plume samples.

of particulate ^{230}Th is found in the large size fraction than ^{234}Th (Fig. 3). Linear regression of fLSF of ^{234}Th against fLSF of ^{230}Th from the entire GP16 section ($n = 44$ samples) reveals an intercept of 0, but a slope of 0.77 ± 0.09 ($r^2 = 0.63$), indicating consistently higher fLSF of ^{230}Th (Fig. 4). This could be explained by the kinetics of adsorption and desorption being more rapid than those of aggregation-disaggregation, as ^{234}Th would have decreased via radioactive decay to lower activities during the aggregation of the SSF into large particles much more so than ^{230}Th, leaving more ^{230}Th in the LSF than ^{234}Th. Since there is limited sampling of ^{230}Th and ^{228}Th in the >51 μm size fraction, inverse models of particle cycling must assume identical size partitioning of the different thorium isotopes to calculate the bulk (SSF + LSF) particulate activities of these isotopes (Lerner et al., 2016, 2017). More measurements of ^{230}Th and ^{228}Th in the LSF would be highly beneficial for further constraining the differential size partitioning of thorium isotopes and its effect on models of particle cycling.

At stations 18–21, there are 17 measurements of particulate ^{230}Th in the LSF in the depth range of the hydrothermal plume. The slope of the regression between fLSF of ^{234}Th against fLSF of ^{230}Th for these samples is 0.9 ± 0.24 – much closer to the expected 1:1 line than for samples collected outside the plume (Fig. 4). While the difference in slopes is not statistically significant, these results are still suggestive that particle aggregation at station 20, and in general the near-axis hydrothermal plume, is more rapid than in the typical deep ocean. Rapid particle aggregation is consistent with the enrichment of fLSF for pFe, pMn, and bulk suspended particulate matter (SPM) in the hydrothermal plume relative to samples taken above the plume at stations 18 and 20 (Lee et al., 2018). The similar size partitioning of ^{234}Th and ^{230}Th within the plume also indicates that the greater depletion of total ^{230}Th than total ^{234}Th in the plume cannot be due to differential incorporation of ^{230}Th into faster sinking particles.

4.2. Scavenging intensity of thorium

The paradigm for understanding ^{230}Th cycling in the ocean is reversible scavenging, whereby thorium reversibly exchanges between the dissolved phase and a small, slow-sinking particulate phase, resulting in the linear increase of both dissolved and particulate ^{230}Th activities with depth (Bacon and Anderson, 1982). In this model, the ratio of particulate thorium activity (A_p) to dissolved thorium activity (A_d), or K_{Th}, is a function of the relative rates of dissolved thorium adsorption onto particles (k_1), desorption and remineralization of thorium from particles into solution (k_{-1}), and the radioactive decay constant (λ):

$$K_{Th} = \frac{A_p}{A_d} = \frac{k_1}{\lambda + k_{-1}} \quad (4)$$

In the reversible scavenging model, variations in K for a given isotope would be due to changes in the relative rates of adsorption and desorption. For ^{230}Th, the decay constant is negligible, so Equation (4) can be simplified to $K = k_1/k_{-1}$.

Because this conceptualization of K does not include sinking losses of particulate thorium, we compute K using only the ratio of small particulate thorium activity to dissolved thorium activity. We find that K values increase for all of the thorium isotopes in the hydrothermal plume (Fig. 5). K is consistently higher for ^{230}Th than for the two shorter-lived isotopes, which is reasonable given that the decay constants for ^{230}Th, ^{228}Th, and ^{234}Th are 9.1×10^{-6} yr^{-1}, 0.36 yr^{-1}, and 10 yr^{-1}, respectively. Thus, if k_1 and k_{-1} are the same for all the thorium isotopes, we would expect K to be largest for ^{230}Th, and smallest for ^{234}Th. However, the K values of ^{234}Th and ^{228}Th are similar to each other both above and within the hydrothermal plume. For average deep ocean values of $k_1 = 0.71$ yr^{-1}, and $k_{-1} = 2.7$ yr^{-1} (Lerner et al., 2017), we would expect to observe K values of 0.27 for ^{230}Th, 0.23 for ^{228}Th, and 0.05 for ^{234}Th. We note that the average values of Lerner et al. (2017) are for the deep North Atlantic, and may be somewhat

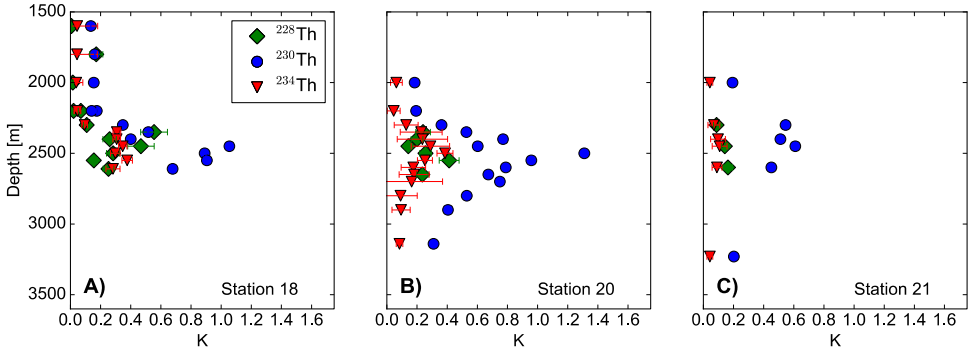

Fig. 5. Particulate (SSF only) to dissolved ratios (K) of ^{228}Th (green diamonds), ^{230}Th (blue circles), and ^{234}Th (red upside-down triangles) at GP16 stations 18 (A), 20 (B), and 21 (C). Uncertainties are 1-sigma and are smaller than the symbol size where not visible.

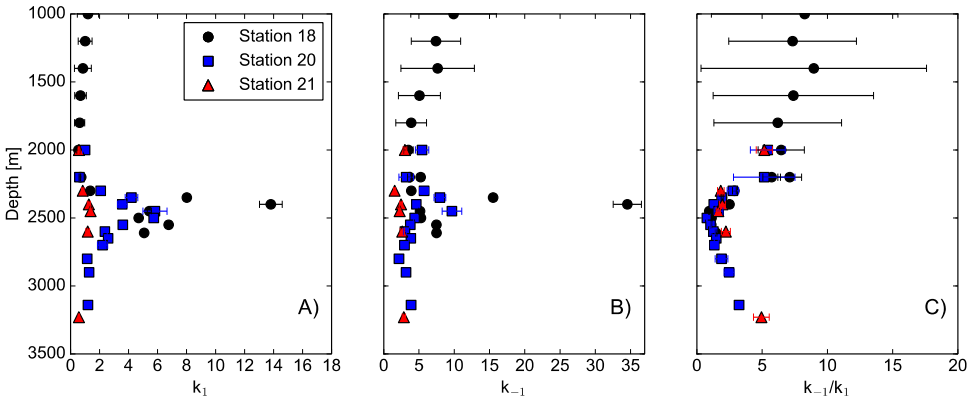

Fig. 6. Adsorption (A) and desorption (B) rate constants (yr^{-1}) for thorium cycling on the GP16 section, as well as the desorption/adsorption rate constant ratio (C). Rate constants are calculated by plugging measured K values for both ^{234}Th and ^{230}Th into Equation (4) (Bacon and Anderson, 1982).

different in the South Pacific. These estimates are still close to observations for ^{230}Th and ^{234}Th, but the observed K values for ^{228}Th are much smaller than predicted, closer to those of ^{234}Th (Fig. 5). This may be an artifact of the measurement method, which can only detect surface adsorbed ^{228}Th. If there is additional ^{228}Th inside particles, perhaps as the result of metal oxide co-precipitation during hydrothermal plume particle formation, this would result in higher K values for ^{228}Th.

We can use Equation (4) to calculate k_1 and k_{-1} values at each station using the measured K values for both ^{230}Th and ^{234}Th (Bacon and Anderson, 1982). We find increases in both adsorption and desorption rate constants from 2400 m–2500 m at stations 18 and 20 (Fig. 6), similar to increases in both rate constants found at the TAG hydrothermal vent site in the North Atlantic (Lerner et al., 2017). However, below 2500 m, the depth of this sharp increase, adsorption and desorption rates rapidly decline, the desorption rates falling below values above the plume, and the ratio of k_{-1}/k_1 reaches a minimum (Fig. 6).

Reversible scavenging assumes that suspended deep ocean particles are at a steady state between adsorption of Th and desorption plus decay of Th. However, Bacon and Anderson (1982) also propose a hybrid model where the adsorption of Th is balanced by decay, desorption, and incorporation of Th into a fast sinking flux, the third process accomplished by the aggregation of small particles into large, faster sinking particles. At stations 18 and 20, both bulk (SSF + LSF) and LSF SPM within the plume are strongly elevated over background levels outside the plume (Lam et al., 2018), generating conditions where particle sinking could be rapid enough to affect the steady state balance of thorium isotopes. Under these conditions, the ratio of particulate to dissolved thorium activity would be described as:

$$K_{\mathrm{Th}} = \frac{k_1}{\lambda + k_{-1} + k_2} \tag{5}$$

where the new term k_2 is the rate constant for the rapid removal of small particulate Th by aggregation into rapidly settling large particles. Since we compute K only using 0.8–51 μm particles, the k_2 term is equivalent to an aggregation rate for the conversion of 0.8–51 μm particles into >51 μm particles. Given the faster particle aggregation inferred from the similar size partitioning of ^{234}Th and ^{230}Th in the hydrothermal plume (Section 4.1), it is likely that particle aggregation is a significant loss term in the budget of small particulate thorium. Thus, k_{-1} values we derived using Equation (4) are in reality a combination of the desorption rate constant and the particle aggregation rate constant. This would imply even lower values for the desorption rate constant than what were previously inferred, especially at stations 18 and 20 where fLSF of particulate Th isotopes is highest.

The controls on Th desorption rate are poorly understood. Values we compute for k_{-1} on GP16 are lower than average values in the deep North Atlantic ocean (e.g. Lerner et al., 2017), especially when the additional effect of particle aggregation is considered. We argue that lower desorption rates are a consequence of a portion of dissolved Th being scavenged irreversibly. Thousands of kilometers west of Station 21, where most of the high mass of pMn has been removed, K values for ^{230}Th and ^{231}Pa remain anomalously high and Th/Pa fractionation factors are anomalously low with respect to the background deep ocean, and close to the endmember values of particulate manganese and iron scavenging (Pavia et al., 2018). One possibility is that Th simply binds to some Fe and Mn particles irreversibly. Another hypothesis is that the production of new Mn and Fe surfaces on particles creates a physical barrier between seawater and solutes already bound to the

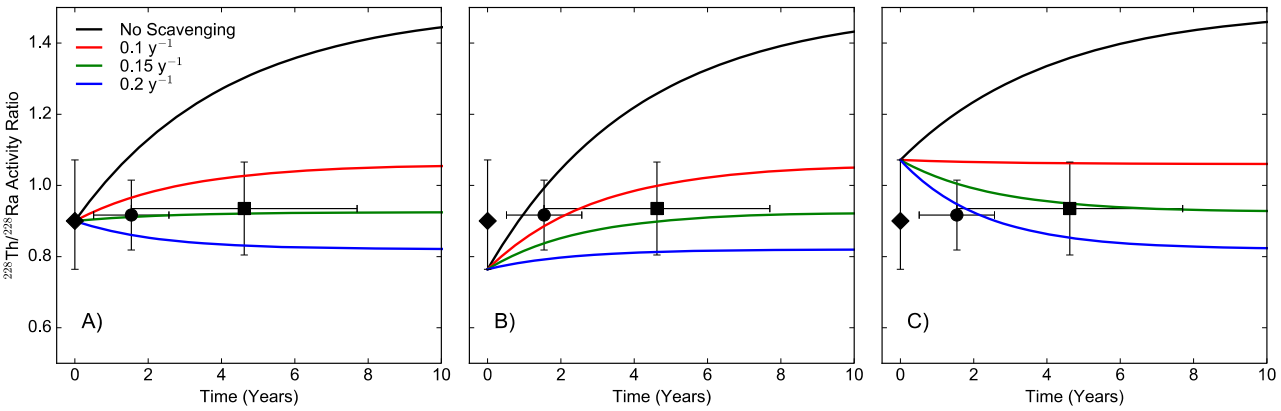

Fig. 7. Observed and modeled total (dissolved + particulate) ^{228}Th/^{228}Ra activity ratios in the hydrothermal plume for a range of initial ^{228}Th and ^{228}Ra activities. Panel A) shows the modeled evolution of ^{228}Th/^{228}Ra using the mean values of ^{228}Ra and ^{228}Th below 2400 m at station 18 as initial activities in Equations (7) and (8). Panel B) shows the same model, but with the lower bound of the ^{228}Th/^{228}Ra ratio at station 18 as the initial activities, and Panel C) shows the same model with the upper bound of ^{228}Th/^{228}Ra at station 18 as the initial activities. The solid lines represent the modeled ^{228}Th/^{228}Ra activity ratio in for a range of scavenging rate constants: black is the no scavenging scenario ($\lambda_s = 0$ yr^{-1} in Equation (8)), red is $\lambda_s = 0.1$ yr^{-1}, green is $\lambda_s = 0.15$ yr^{-1}, and blue is $\lambda_s = 0.2$ yr^{-1}. Mean observed total ^{228}Th/^{228}Ra activity ratios within the hydrothermal plume at stations 18, 20, and 21 and their 1-sigma uncertainties are shown as diamonds, circles, and squares, respectively. Plume ages and their uncertainties at stations 20 and 21 are derived from ^{227}Ac measurements and physical oceanographic estimates of flow velocities (see Section 4.3).

particle, preventing desorption back into solution and resulting in the irreversible scavenging of Th. Additional research is required to discriminate between these two possibilities.

4.3. Variable depletion among the Th isotopes

Measurements of the three thorium isotopes can be used to study the kinetics of scavenging in the early history of the hydrothermal plume. Total ^{230}Th is highly depleted in the plume relative to reversible scavenging, while total ^{234}Th is nearly in secular equilibrium with its parent ^{238}U. This difference informs us about the time scale for scavenging and removal.

We can quantify the percent depletion of any thorium isotope at a given depth by the following equation (Lopez et al., 2015; Pavia et al., 2018):

$$Percent\ Depletion = \frac{A_{pred} - A_{obs}}{A_{pred}} \times 100 \quad (6)$$

where A_{pred} is the predicted total (dissolved + bulk particulate) activity of a Th isotope, and A_{obs} is the observed total activity. Given the need to use total activities, and the lack of ^{230}Th and ^{228}Th measurements in the large size fraction for every sample, we multiply SSF activities of ^{230}Th (where there are no measurements in the LSF) and ^{228}Th by the LSF/SSF activity ratio observed for ^{234}Th for a given sample to estimate the LSF contribution to the total ^{228}Th and ^{230}Th for that sample.

For ^{234}Th, the predicted activity is that of its parent isotope ^{238}U (secular equilibrium). For ^{230}Th, the predicted activity is derived by extrapolating the increase in activity with depth above the hydrothermal plume into the observed depths within the hydrothermal plume, as expected from reversible scavenging (Bacon and Anderson, 1982; Lopez et al., 2015; Pavia et al., 2018).

For ^{228}Th, the predicted activity is more complicated. Since the half-life of ^{228}Th is only slightly shorter than that of its parent ^{228}Ra, in a closed system ^{228}Th will approach a transient equilibrium with ^{228}Ra where ^{228}Th/^{228}Ra activity ratios reach 1.5 (e.g. Turekian et al., 1975). This behavior has been modeled in studies of shelf-basin exchange and scavenging dynamics (Kipp et al., 2018a; Rutgers van der Loeff et al., 2012, 2018). We adapt these models for use in the GP16 hydrothermal plume. For a purely advective system, once hydrothermal supply of ^{228}Ra has ceased, ^{228}Ra activities will change only as a function of radioactive decay over time (t):

$$^{228}\mathrm{Ra}(t) = {}^{228}\mathrm{Ra}_0 e^{-\lambda_{228} t} \quad (7)$$

In this and the following equation, the subscript $_0$ indicates initial activity at the time when the hydrothermal plume leaves the ridge. The activity of ^{228}Th at time t is a function of ingrowth, decay, and scavenging (Kipp et al., 2018a; Rutgers van der Loeff et al., 2012, 2018):

$$^{228}\mathrm{Th}(t) = {}^{228}\mathrm{Th}_0 e^{-(\lambda_{\mathrm{Th}}+\lambda_s)t} + \frac{\lambda_{\mathrm{Th}}}{\lambda_{\mathrm{Th}} + \lambda_s - \lambda_{\mathrm{Ra}}} {}^{228}\mathrm{Ra}_0 \left(e^{-\lambda_{\mathrm{Ra}} t} - e^{-(\lambda_{\mathrm{Th}}+\lambda_s)t}\right) \quad (8)$$

where λ_{Th} and λ_{Ra} are the decay constants of ^{228}Th and ^{228}Ra, and λ_s is the ^{228}Th scavenging rate constant. This model neglects the impacts of lateral and vertical mixing on ^{228}Th and ^{228}Ra, and requires knowledge of the initial ^{228}Th and ^{228}Ra activities at the time the plume advects away from the ridge axis. We use the ^{228}Ra and ^{228}Th activities at station 18 as the initial values to predict ^{228}Th/^{228}Ra ratios at stations 20 and 21. Plume ages (t) at stations 18 and 20 were determined using a wide range of off-axis flow velocities in the hydrothermal plume of 0.1–0.5 cm/s based on dilution-corrected ^{227}Ac decay (Hammond et al., 2016; Lupton and Jenkins, 2017), neutrally buoyant floats (Lupton and Jenkins, 2017), and inverse modeling (Faure and Speer, 2012; Hautala and Riser, 1993). These flow velocities, multiplied by the distances of stations 20 (81 km) and 21 (243 km) from the ridge, yield plume ages of 0.5–2.6 yr at station 20, and 1.5–7.7 yr at station 21.

The best-fit off-axis scavenging rate for the measured ^{228}Th/^{228}Ra ratios at stations 20 and 21 is 0.15 yr^{-1} (Fig. 7). The mean ratio of ^{228}Th/^{228}Ra activities below 2400 m at station 18 is 0.9. The best-fit scavenging rate of 0.15 is relatively insensitive to the initial ^{228}Th/^{228}Ra ratio, consistent with the upper and lower error bounds of the ^{228}Th/^{228}Ra ratio at station 18 – varying only by ~0.05 yr^{-1} for the range of initial ^{228}Th/^{228}Ra ratios at station 18 (Figs. 7B and 7C). Since the ^{228}Th/^{228}Ra ratios at stations 18–21 are relatively invariant, and the scavenging rate of 0.15 yr^{-1} results in a nearly constant ^{228}Th/^{228}Ra ratio over time, our results are also insensitive to uncertainties in the plume ages. While we do not take mixing into account, the effect of lateral mixing on the ^{228}Th/^{228}Ra ratios should also be minimal, since ^{228}Th and ^{228}Ra activities are both a factor of 2–3 higher in the hydrothermal plume than in overlying waters, which we take to be

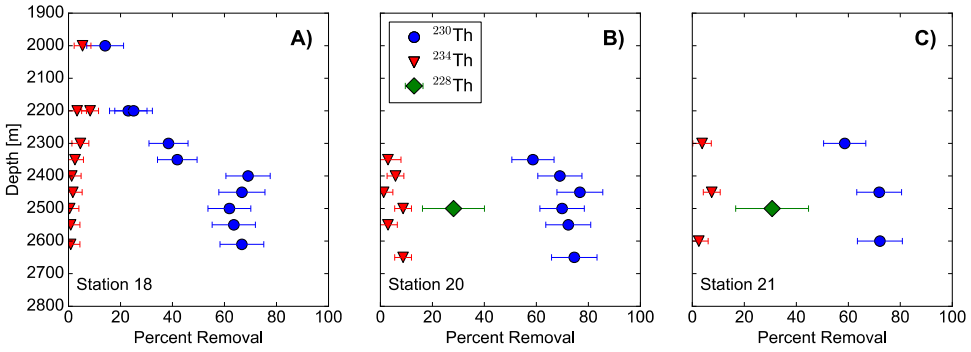

Fig. 8. Percent removal for total pools of ^{234}Th (red upside-down triangles), ^{228}Th (green diamonds), and ^{230}Th (blue circles) at stations 18 (A), 20 (B), and 21 (C). Uncertainties shown are 1-sigma. Station 18 is used to constrain the initial conditions for the ^{228}Th–^{228}Ra pair, so there is no percent removal value for ^{228}Th shown in (A).

representative of background, non-plume waters (Fig. 2C). The off-axis hydrothermal Th scavenging rate constant of 0.15 ± 0.05 yr^{-1} will be useful for future studies of off-axis scavenging dynamics.

We can use the no scavenging scenario (solid black lines in Fig. 7, $\lambda_s = 0$ in Equation (8)) to determine the percent depletion of ^{228}Th at stations 20 and 21, but not station 18, since we initiate the model using the ^{228}Th/^{228}Ra ratios from station 18. In Equation (6), A_{pred} is the ^{228}Th/^{228}Ra ratio of the no scavenging scenario (dashed line in Fig. 7C) at the age of the plume at a given station, and A_{obs} is the averaged observed ^{228}Th/^{228}Ra ratio at that station. The percent depletion is thus averaged within the plume, and we display the average value at 2500 m in Fig. 8.

Depletion of total ^{230}Th in the hydrothermal plume relative to that predicted by extrapolating trends above 2000 m reaches a maximum of 70% at stations 18–20 (Fig. 8). At those stations, total ^{234}Th is only depleted a maximum of 8%. Depletion of total ^{228}Th is 28 ± 12% at station 20 and 31 ± 14% at station 21. Scavenging occurring over 100 days in the past would have a negligible lasting imprint on ^{234}Th, but ^{230}Th and ^{228}Th would largely retain the signal of scavenging. Greater depletion of ^{230}Th and ^{228}Th than ^{234}Th at those stations could indicate that the majority of the Th was scavenged and removed from seawater over 100 days prior to sampling, long enough for ^{234}Th to have nearly returned to its predicted value of secular equilibrium.

If this early scavenging history were true, and the scavenging was the result of the most recent input of hydrothermal materials, then we might expect the scavenging signals of the three thorium isotopes to be coherent at station 18, which was sampled directly above the EPR, though not necessarily above an active vent. Station 18 had measurable ^{223}Ra ($t_{1/2} = 11.4$ days), meaning that there had been a recent input of hydrothermal fluids. However, there was no hydrothermal ^{224}Ra ($t_{1/2} = 3.66$ days), which is enriched in high-temperature vent fluids (Kipp et al., 2018b), indicating that the plume was at least 18 days (five ^{224}Ra half-lives) old. Using a range of ^{223}Ra/^{226}Ra ratios observed in vent fluids, Kipp et al. (2018b) constrained the age of the hydrothermal plume at Station 18 to be 24–32 days. However, it is possible that hydrothermal activity >50 days in the past could have injected additional ^{226}Ra, which would decrease the apparent age of the plume since any additional ^{223}Ra injected would have decayed away. Thus we suggest that a more appropriate age range of the hydrothermal plume at station 18 is 18–32 days. Future surveys of Ra injection along the EPR may be able to confirm where and when additional hydrothermal ^{226}Ra is added as waters flow northward above the ridge.

At station 18, the depletion of ^{230}Th reaches 70%, while the maximum depletion of ^{234}Th is 8%. Given that the 18–32 day age of the plume is similar to the half-life of ^{234}Th, if the two Th isotopes had been removed to the same degree at the EPR crest 18–32 days prior to sample collection, then a far greater depletion of ^{234}Th should be observed. Below, we model the time evolution of Th isotopes following a scavenging event to specifically test whether our data are consistent with a single recent scavenging event being responsible for the 8% depletion of total ^{234}Th and 70% depletion of ^{230}Th at station 18.

The mass balance of a radioactive daughter isotope (denoted here N_2, in atoms) of a given parent (N_1, in atoms) following scavenging removal can be written from the Bateman equations for radioactive decay as follows:

$$\frac{dN_2}{dt} = \lambda_1 N_1^0 e^{-\lambda_1 t} - \lambda_2 N_2 \tag{9}$$

where λ is the decay constant of the isotope, N_1^0 indicates the initial atoms of the parent isotope present, and t is time elapsed since a scavenging event early in the history of the hydrothermal plume. This equation can be solved for the number of N_2 daughter atoms present at time t:

$$N_2(t) = \frac{\lambda_1}{\lambda_2 - \lambda_1} N_1^0 \left(e^{-\lambda_1 t} - e^{-\lambda_2 t}\right) + N_2^0 e^{-\lambda_2 t} \tag{10}$$

The first term on the right side of the Equation (10) is the number of N_2 atoms present that have ingrown from its parent N_1, but have not yet undergone radioactive decay. The second term on the right side of the equation is the loss by radioactive decay of the daughter nuclide initially present immediately after the scavenging event. We can use this model to assess the depletion that ought to be observed if ^{234}Th experienced the same 70% depletion as ^{230}Th at the upper age limit of the plume age (32 days) derived from ^{223}Ra/^{226}Ra dating – the most conservative possible condition, allowing the most time for ^{234}Th ingrowth from U decay. If ^{234}Th was 70% depleted 32 days before sampling, there should have been a 30% deficit in ^{234}Th observed at station 18 (dashed line in Fig. 9), far greater than the observed maximum of 8% depletion.

If we assume that 70% depletion of ^{234}Th did occur and that the plume age is an unknown variable, then we can solve for the minimum amount of time that must have elapsed for 8% depletion to be observed at station 18. For 8% depletion to be measured at station 18, 70% removal of ^{234}Th would have to have happened 75 days prior to sampling (dotted line in Fig. 9). The observed ^{223}Ra$_{xs}$/^{226}Ra ratio at station 18 of 0.011 and a 75 day old plume would require a vent fluid ^{223}Ra/^{226}Ra activity of 1.09, which is both 2–3 times larger than the maximum ^{223}Ra/^{226}Ra ratios ever measured in vent fluids, and over an order of magnitude larger than the average vent fluid ^{223}Ra/^{226}Ra ratio (Kipp et al., 2018b). It is also an order of magnitude higher than ^{231}Pa/^{226}Ra activity ratios measured in basalts from the EPR, which, at steady state, set the ^{223}Ra/^{226}Ra ratios of vent fluids (Bourdon et al., 2000; Lundstrom et al., 1999; Sims et al., 2002). The decoupling of ^{234}Th depletion and ^{230}Th depletion could be explained if ^{230}Th had pre-existing depletion due to scavenging that had occurred before the

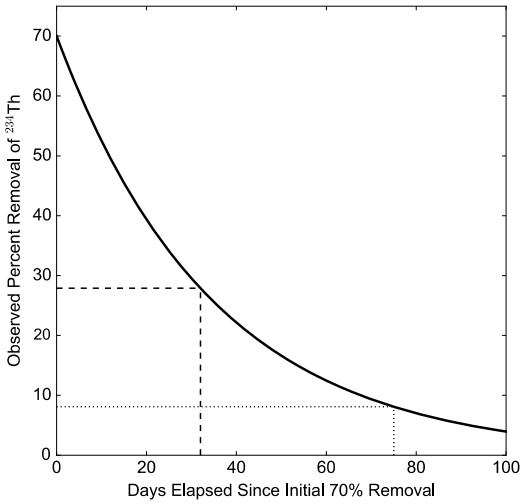

Fig. 9. Modeled ^{234}Th depletion (y-axis) as a function of elapsed time after a 70% depletion (maximum observed ^{230}Th depletion relative to reversible scavenging) of ^{234}Th (x-axis). The dashed line corresponds to the predicted depletion of ^{234}Th if 70% scavenging had occurred 32 days previously, the upper limit for the age of the plume at Station 18. The dotted line marks the time necessary to have elapsed for an 8% depletion of ^{234}Th to be observed at station 18.

most recent injection of hydrothermal material prior to sampling at station 18.

Finally, we rearrange Equation (10) to solve for the maximum initial removal of ^{234}Th (N_2^0) in the early history of the hydrothermal plume:

$$N_2^0 = \frac{N_2(t) - \frac{\lambda_1}{\lambda_2 - \lambda_1} N_1^0 (e^{-\lambda_1 t} - e^{-\lambda_2 t})}{e^{-\lambda_2 t}} \quad (11)$$

We find that an 18–32 day plume age and maximum observed depletion of ^{234}Th of 8% at station 18 would require the instantaneous Th removal of 14–20% since the water mass encountered the vent source of the hydrothermal plume, much less than the 70% observed depletion of ^{230}Th at station 18. Given the enrichment of particulate ^{234}Th at station 18 but lack of total depletion, it is likely that particle aggregation and sinking occurs on timescales greater than the half-life of ^{234}Th, so instantaneous 14–20% depletion of ^{234}Th at a vent is an endmember scenario rather than a requirement of our model. Regardless, we have shown that the 70% depletion of ^{230}Th cannot be explained by a single recent scavenging event, indicating that ^{230}Th has an inherited scavenging signal, most reasonably from hydrothermal activity preceding the most recent scavenging event.

Float trajectories and modeling studies suggest topographically-steered equatorward flow extending hundreds of meters above the EPR ridge axis from 40°S to 10°S, with velocities of 0.2–0.5 cm/s (Hautala and Riser, 1993; Zilberman et al., 2017). This flow passes across a number of active high-temperature hydrothermal vents just south of our study area (Fig. 1). Previous surveys documented particularly intense hydrothermal activity between 17°S–19°S, with Fe- and Mn-rich particle-laden plumes in the water column (Feely et al., 1996; Urabe et al., 1995). Resing et al. (2015) suggested that the dFe and dMn enrichment in the GP16 plume at station 20 and westward was from these 17°S–19°S vent fields. Jenkins et al. (2018) suggested that the ^{3}He in the GP16 plume may have been sourced from further south as well, since the ^{3}He and ^{4}He were correlated with a slope of 9.04 ± 0.24 R/R_a (^{3}He/^{4}He ratio relative to the atmospheric ratio), higher than the typical MORB value of 8 R/R_a, and consistent with high ^{3}He/^{4}He of 9–11 R/R_a in EPR basalts at 17°S (Kurz et al., 2005). We hypothesize that much of the 70% depletion of ^{230}Th observed in the GP16 hydrothermal plume is due to scavenging in the particle-rich plumes of this 17°S–19°S region, which then veered west towards stations 20 and 21 (dashed white arrow in Fig. 1).

If the ^{230}Th removal rates were greater than the integrated production rate from U decay in the overlying water column, it would require a lateral diffusive source of ^{230}Th, making this portion of the EPR a boundary sink for ^{230}Th, and potentially biasing the near- and off-axis application of sedimentary ^{230}Th-normalization for determining mass accumulation rates (e.g. Bacon, 1984; Francois et al., 2004) in the South Pacific at these latitudes. More research is required to determine the effect of hydrothermal activity on sedimentary ^{230}Th burial rates.

5. Conclusions

Combined measurements of dissolved and particulate ^{234}Th, ^{230}Th, and ^{228}Th allowed us to better understand the kinetics of hydrothermal plume particle dynamics and scavenging in the South Pacific Ocean. The size partitioning of ^{234}Th and ^{230}Th between >51 μm and 0.8–51 μm particles was more closely coupled in the hydrothermal plume than for typical waters from the rest of the section, indicating that particle aggregation was occurring much more rapidly in the plume. By determining adsorption and desorption rate constants for thorium, in combination with the finding of rapid particle aggregation, we hypothesize that hydrothermal scavenging is partially irreversible.

Modeling the evolution of ^{228}Th/^{228}Ra ratios revealed an off-axis hydrothermal Th scavenging rate of 0.15 yr^{-1}. We found variable removal among the three Th isotopes in the near-axis plume, with ^{230}Th the most depleted, followed by ^{228}Th, then ^{234}Th. The large degree of ^{230}Th removal is inconsistent with a single local scavenging event, and is more likely due to progressive scavenging in the region of intense hydrothermal activity from 17°S to 19°S.

These results illustrate the complexity of interpreting the GP16 hydrothermal plume as being solely a local phenomenon. The time information provided by the radioactivity of the thorium isotopes shows that the scavenging signals observed in the GP16 section are a result of hydrothermal activity further south on the EPR. Future studies combining data from multiple radiogenic thorium isotopes in this manner will be useful for understanding the time dynamics from other parts of the GP16 section, such as the upper water column, the continental shelf, and benthic nepheloid layers.

Acknowledgements

This work was supported by the U.S. National Science Foundation (OCE-1233688 to LDEO, OCE-1233903 to UMN), OCE-1232669 to WHOI, OCE-1231211 to USC) and an NSF Graduate Research Fellowship to F.J.P. (DGE-16-44869). We thank the captain, crew, and scientists aboard the R/V Thomas G. Thompson. Constructive comments from three anonymous reviewers greatly improved the quality of this manuscript. We are grateful to John Lupton for sharing Helios float trajectories, Ken Buesseler for overseeing the collection of the ^{234}Th data, and to Phoebe Lam and Kassandra Costa for helpful discussions.

References

Andersen, M.B., Stirling, C.H., Zimmermann, B., Halliday, A.N., 2010. Precise determination of the open ocean ^{234}U/^{238}U composition. Geochem. Geophys. Geosyst. 11. https://doi.org/10.1029/2010GC003318.

Bacon, M.P., 1984. Glacial to interglacial changes in carbonate and clay sedimentation in the Atlantic Ocean estimated from ^{230}Th measurements. Chem. Geol. 46, 97–111. https://doi.org/10.1016/0009-2541(84)90183-9.

Bacon, M.P., Anderson, R.F., 1982. Distribution of thorium isotopes between dissolved and particulate forms in the deep sea. J. Geophys. Res. 87, 2045–2056. https://doi.org/10.1111/j.1365-3091.2012.01327.x.

Black, E.E., Buesseler, K.O., Pike, S.M., Lam, P.J., 2018. ^{234}Th as a tracer of particulate export and remineralization in the southeastern tropical Pacific. Mar. Chem. 201, 35–50. https://doi.org/10.1016/j.marchem.2017.06.009.

Bourdon, B., Goldstein, S.J., Bourles, D., Murrell, M.T., Langmuir, C.H., 2000. Evidence from ^{10}Be and U series disequilibria on the possible contamination of mid-ocean ridge basalt glasses by sedimentary material. Geochem. Geophys. Geosyst. 1. https://doi.org/10.1029/2000GC000047.

Burd, A.B., Jackson, G.A., 2009. Particle aggregation. Annu. Rev. Mar. Sci. 1, 65–90. https://doi.org/10.1146/annurev.marine.010908.163904.

Charette, M.A., Morris, P.J., Henderson, P.B., Moore, W.S., 2015. Radium isotope distributions during the US GEOTRACES North Atlantic cruises. Mar. Chem. 177, 184–195. https://doi.org/10.1016/j.marchem.2015.01.001.

Cheng, H., Edwards, R.L., Shen, C.-C., Polyak, V.J., Asmerom, Y., Woodhead, J., Hellstrom, J., Wang, Y., Kong, X., Spötl, C., Wang, X., Alexander Jr., E. Calvin, 2013. Improvements in ^{230}Th dating, ^{230}Th and ^{234}U half-life values, and U–Th isotopic measurements by multi-collector inductively coupled plasma mass spectrometry. Earth Planet. Sci. Lett. 371–372, 82–91. https://doi.org/10.1016/j.epsl.2013.04.006.

Faure, V., Speer, K., 2012. Deep circulation in the Eastern South Pacific Ocean. J. Mar. Res. 70, 748–778. https://doi.org/10.1357/002224012806290714.

Feely, R.A., Baker, E.T., Marumo, K., Urabe, T., Ishibashi, J., Gendron, J., Lebon, G.T., Okamura, K., 1996. Hydrothermal plume particles and dissolved phosphate over the superfast-spreading southern East Pacific Rise. Geochim. Cosmochim. Acta 60, 2297–2323. https://doi.org/10.1016/0016-7037(96)00099-3.

Feely, R.A., Geiselman, T.L., Baker, E.T., Massoth, G.J., Hammond, S.R., 1990. Distribution and composition of hydrothermal plume particles from the ASHES Vent Field at Axial Volcano, Juan de Fuca Ridge. J. Geophys. Res., Oceans (1978–2012) 95, 12855–12873. https://doi.org/10.1029/JB095iB08p12855.

Feely, R.A., Lewison, M., Massoth, G.J., Baldo, G.R., Lavelle, J.W., Byrne, R.H., Von Damm, K.L., Curl, H.C., 1987. Composition and dissolution of black smoker particulates from active vents on the Juan de Fuca Ridge. J. Geophys. Res., Oceans (1978–2012) 92, 11347–11363. https://doi.org/10.1029/JB092iB11p11347.

Fitzsimmons, J.N., John, S.G., Marsay, C.M., Hoffman, C.L., Nicholas, S.L., Toner, B.M., German, C.R., Sherrell, R.M., 2017. Iron persistence in a distal hydrothermal plume supported by dissolved-particulate exchange. Nat. Geosci. 10, 195–201. https://doi.org/10.1038/ngeo2900.

Francois, R., Frank, M., Rutgers van der Loeff, M.M., Bacon, M.P., 2004. ^{230}Th normalization: an essential tool for interpreting sedimentary fluxes during the late Quaternary. Paleoceanography 19. https://doi.org/10.1029/2003PA000939.

German, C.R., Legendre, L.L., Sander, S.G., Niquil, N., Luther III, G.W., Bharati, L., Han, X., Le Bris, N., 2015. Hydrothermal Fe cycling and deep ocean organic carbon scavenging: model-based evidence for significant POC supply to seafloor sediments. Earth Planet. Sci. Lett. 419, 143–153. https://doi.org/10.1016/j.epsl.2015.03.012.

German, C.R., Seyfried, W.E., 2014. Hydrothermal processes. In: Holland, H.D., Turekian, K.K. (Eds.), Treatise on Geochemistry. Elsevier Ltd., pp. 191–233.

Hammond, D.E., Charette, M.A., Moore, W.S., Henderson, P., Sanial, V., Kipp, L.E., Anderson, R.F., Primeau, F., 2016. ^{227}Ac in the Deep South Pacific along the Peru–Tahiti GEOTRACES Transect: mixing and transport rates. In: Ocean Sciences Meeting 2016. American Geophysical Union. Abstract #CT14B-0138.

Hautala, S.L., Riser, S.C., 1993. A nonconservative β-spiral determination of the deep circulation in the Eastern South Pacific. J. Phys. Oceanogr. 23, 1975–2000. https://doi.org/10.1175/1520-0485(1993)023<1975:ansdot>2.0.co;2.

Henderson, G.M., Anderson, R.F., 2003. The U-series toolbox for paleoceanography. Rev. Mineral. Geochem. 52, 493–531. https://doi.org/10.2113/0520493.

Henderson, P.B., Morris, P.J., Moore, W.S., Charette, M.A., 2013. Methodological advances for measuring low-level radium isotopes in seawater. J. Radioanal. Nucl. Chem. 296, 357–362. https://doi.org/10.1007/s10967-012-2047-9.

Honeyman, B.D., Santschi, P.H., 1989. A Brownian-pumping model for oceanic trace metal scavenging: evidence from Th isotopes. J. Mar. Res. 47, 951–992. https://doi.org/10.1357/002224089785076091.

Jenkins, W.J., Lott III, D.E., German, C.R., Cahill, K.L., Goudreau, J., Longworth, B., 2018. The deep distributions of helium isotopes, radiocarbon, and noble gases along the U.S. GEOTRACES East Pacific Zonal Transect (GP16). Mar. Chem. 201, 167–182. https://doi.org/10.1016/j.marchem.2017.03.009.

Kadko, D., 1996. Radioisotopic studies of submarine hydrothermal vents. Rev. Geophys. 34, 349–366. https://doi.org/10.1029/96RG01762.

Kadko, D., Feely, R., Massoth, G., 1994. Scavenging of ^{234}Th and phosphorus removal from the hydrothermal effluent plume over the North Cleft segment of the Juan de Fuca Ridge. J. Geophys. Res., Oceans (1978–2012) 99, 5017–5024. https://doi.org/10.1029/93JB02952.

Kipp, L.E., Charette, M.A., Moore, W.S., Henderson, P.B., Rigor, I.G., 2018a. Increased fluxes of shelf-derived materials to the central Arctic Ocean. Sci. Adv. 4, eaao1302. https://doi.org/10.1126/sciadv.aao1302.

Kipp, L.E., Sanial, V., Henderson, P.B., van Beek, P., Reyss, J.-L., Hammond, D.E., Moore, W.S., Charette, M.A., 2018b. Radium isotopes as tracers of hydrothermal inputs and neutrally buoyant plume dynamics in the deep ocean. Mar. Chem. 201, 51–65. https://doi.org/10.1016/j.marchem.2017.06.011.

Kirby, H.W., Grove, G.R., Timma, D.L., 1956. Neutron-capture cross section of actinium-227. Phys. Rev. 102, 1140. https://doi.org/10.1103/PhysRev.102.1140.

Knight, G.B., Macklin, R.L., 1948. Half-life of U X1(Th234). Phys. Rev. 74, 1540–1541. https://doi.org/10.1103/PhysRev.74.1540.

Kurz, M.D., Moreira, M., Curtice, J., Lott III, D.E., Mahoney, J.J., Sinton, J.M., 2005. Correlated helium, neon, and melt production on the super-fast spreading East Pacific Rise near 17°S. Earth Planet. Sci. Lett. 232, 125–142. https://doi.org/10.1016/j.epsl.2005.01.005.

Lam, P.J., Lee, J.M., Heller, M.I., Mehic, S., Xiang, Y., Bates, N.R., 2018. Size-fractionated distributions of suspended particle concentration and major phase composition from the U.S. GEOTRACES Eastern Pacific Zonal Transect (GP16). Mar. Chem. 201, 90–107. https://doi.org/10.1016/j.marchem.2017.08.013.

Lee, J.M., Heller, M.I., Lam, P.J., 2018. Size distribution of particulate trace elements in the U.S. GEOTRACES Eastern Pacific Zonal Transect (GP16). Mar. Chem. 201, 108–123. https://doi.org/10.1016/j.marchem.2017.09.006.

Lerner, P., Marchal, O., Lam, P.J., Anderson, R.F., Buesseler, K., Charette, M.A., Edwards, R.L., Hayes, C.T., Huang, K.-F., Lu, Y., Robinson, L.F., Solow, A., 2016. Testing models of thorium and particle cycling in the ocean using data from station GT11-22 of the U.S. GEOTRACES North Atlantic section. Deep-Sea Res., Part 1, Oceanogr. Res. Pap. 113, 57–79. https://doi.org/10.1016/j.dsr.2016.03.008.

Lerner, P., Marchal, O., Lam, P.J., Buesseler, K., Charette, M., 2017. Kinetics of thorium and particle cycling along the U.S. GEOTRACES North Atlantic Transect. Deep-Sea Res., Part 1, Oceanogr. Res. Pap. 125, 106–128. https://doi.org/10.1016/j.dsr.2017.05.003.

Lopez, G.I., Marcantonio, F., Lyle, M., Lynch-Stieglitz, J., 2015. Dissolved and particulate ^{230}Th–^{232}Th in the Central Equatorial Pacific Ocean: evidence for far-field transport of the East Pacific Rise hydrothermal plume. Earth Planet. Sci. Lett. 431, 87–95. https://doi.org/10.1016/j.epsl.2015.09.019.

Lundstrom, C.C., Sampson, D.E., Perfit, M.R., Gill, J., Williams, Q., 1999. Insights into mid-ocean ridge basalt petrogenesis: U-series disequilibria from the Siqueiros Transform, Lamont Seamounts, and East Pacific Rise. J. Geophys. Res., Oceans (1978–2012) 104, 13035–13048. https://doi.org/10.1029/1999JB900081.

Lupton, J.E., Craig, H., 1981. A major helium-3 source at 15°S on the East Pacific Rise. Science 214, 13–18. https://doi.org/10.1126/science.214.4516.13.

Lupton, J.E., Jenkins, W.J., 2017. Evolution of the south Pacific helium plume over the past three decades. Geochem. Geophys. Geosyst. 18, 1810–1823. https://doi.org/10.1002/2017GC006848.

Maiti, K., Charette, M.A., Buesseler, K.O., Zhou, K., Henderson, P., Moore, W.S., Morris, P., Kipp, L., 2015. Determination of particulate and dissolved ^{228}Th in seawater using a delayed coincidence counter. Mar. Chem. 177, 196–202. https://doi.org/10.1016/j.marchem.2014.12.001.

Moore, W.S., Arnold, R., 1996. Measurement of ^{223}Ra and ^{224}Ra in coastal waters using a delayed coincidence counter. J. Geophys. Res., Oceans (1978–2012) 101, 1321–1329. https://doi.org/10.1029/95JC03139.

Moore, W.S., Sackett, W.M., 1964. Uranium and thorium series inequilibrium in sea water. J. Geophys. Res. 69, 5401–5405. https://doi.org/10.1029/JZ069i024p05401.

Owens, S.A., Buesseler, K.O., Sims, K.W.W., 2011. Re-evaluating the ^{238}U-salinity relationship in seawater: implications for the ^{238}U–^{234}Th disequilibrium method. Mar. Chem. 127, 31–39. https://doi.org/10.1016/j.marchem.2011.07.005.

Owens, S.A., Pike, S., Buesseler, K.O., 2015. Thorium-234 as a tracer of particle dynamics and upper ocean export in the Atlantic Ocean. Deep-Sea Res., Part 2, Top. Stud. Oceanogr. 116, 42–59. https://doi.org/10.1016/j.dsr2.2014.11.010.

Pavia, F., Anderson, R., Vivancos, S., Fleisher, M., Lam, P., Lu, Y., Cheng, H., Zhang, P., Edwards, R.L., 2018. Intense hydrothermal scavenging of ^{230}Th and ^{231}Pa in the deep Southeast Pacific. Mar. Chem. 201, 212–228. https://doi.org/10.1016/j.marchem.2017.08.003.

Resing, J.A., Sedwick, P.N., German, C.R., Jenkins, W.J., Moffett, J.W., Sohst, B.M., Tagliabue, A., 2015. Basin-scale transport of hydrothermal dissolved metals across the South Pacific Ocean. Nature 523, 200–203. https://doi.org/10.1038/nature14577.

Roy-Barman, M., Lemaître, C., Ayrault, S., Jeandel, C., Souhaut, M., Miquel, J.C., 2009. The influence of particle composition on Thorium scavenging in the Mediterranean Sea. Earth Planet. Sci. Lett. 286, 526–534. https://doi.org/10.1016/j.epsl.2009.07.018.

Rutgers van der Loeff, M., Cai, P., Stimac, I., Bauch, D., Hanfland, C., Roeske, T., Moran, S.B., 2012. Shelf-basin exchange times of Arctic surface waters estimated from ^{228}Th/^{228}Ra disequilibrium. J. Geophys. Res., Oceans (1978–2012) 117. https://doi.org/10.1029/2011JC007478.

Rutgers van der Loeff, M., Kipp, L., Charette, M.A., Moore, W.S., Black, E., Stimac, I., Charkin, A., Bauch, D., Valk, O., Karcher, M., Krumpen, T., Casacuberta, N., Smethie, W., Rember, R., 2018. Radium isotopes across the Arctic Ocean show time scales of water mass ventilation and increasing shelf inputs. J. Geophys. Res., Oceans 123, 4853–4873. https://doi.org/10.1029/2018JC013888.

Sims, K.W.W., Goldstein, S.J., Blichert-toft, J., Perfit, M.R., Kelemen, P., Fornari, D.J., Michael, P., Murrell, M.T., Hart, S.R., DePaolo, D.J., Layne, G., Ball, L., Jull, M., Bender, J., 2002. Chemical and isotopic constraints on the generation and transport of magma beneath the East Pacific Rise. Geochim. Cosmochim. Acta 66, 3481–3504. https://doi.org/10.1016/S0016-7037(02)00909-2.

Tagliabue, A., Bopp, L., Dutay, J.-C., Bowie, A.R., Chever, F., Jean-Baptiste, P., Bucciarelli, E., Lannuzel, D., Remenyi, T., Sarthou, G., Aumont, O., Gehlen, M., Jeandel, C., 2010. Hydrothermal contribution to the oceanic dissolved iron inventory. Nat. Geosci. 3, 252–256. https://doi.org/10.1038/ngeo818.

Turekian, K.K., Cochran, J.K., Kharkar, D.P., Cerrato, R.M., Vaisnys, J.R., Sanders, H.L., Grassle, J.F., Allen, J.A., 1975. Slow growth rate of a deep-sea clam determined by ^{228}Ra chronology. Proc. Natl. Acad. Sci. USA 72, 2829–2832. https://doi.org/10.1073/pnas.72.7.2829.

Urabe, T., Baker, E.T., Ishibashi, J., Feely, R.A., Marumo, K., Massoth, G.J., Maruyama, A., Shitashima, K., Okamura, K., Lupton, J.E., Sonoda, A., Yamazaki, T., Aoki, M., Gendron, J., Greene, R., Kaiho, Y., Kisimoto, K., Lebon, G., Matsumoto, T., Nakamura, K., Nishizawa, A., Okano, O., Paradis, G., Roe, K., Shibata, T., Tennant, D., Vance, T., Walker, S.L., Yabuki, T., Ytow, N., 1995. The effect of magmatic activity on hydrothermal venting along the superfast-spreading East Pacific Rise. Science 269, 1092–1095. https://doi.org/10.1126/science.269.5227.1092.

Zilberman, N.V., Roemmich, D.H., Gille, S.T., 2017. The East Pacific Rise current: topographic enhancement of the interior flow in the South Pacific Ocean. Geophys. Res. Lett. 44, 277–285. https://doi.org/10.1002/2016GL069039.